Mitigation of Sawtooth transient heat flux in the MAST-U Super-X Divertor with Deuterium and Nitrogen

Rory Scannell[1], Jack Flanagan[1,2], Zhouji Huang[1], James Harrison[1], Kevin Verhaegh[3], Scott Silburn[1], Peter Ryan [1], Stuart Henderson[1], Nicola Lonigro[1,4], Sid Leigh[1], David Moulton[1], Sam Blackmore[1], and the MAST-U team

1 UKAEA (United Kingdom Atomic Energy Authority), Culham Campus, Abingdon, Oxfordshire, OX14 3DB, UK

2 University of Liverpool, Liverpool, L69 7ZX, UK

3 Eindhoven University of Technology, Eindhoven, The Netherlands

4 York Plasma Institute, University of York, York, YO10 5DD, UK

E-mail: rory.scannell@ukaea.uk

Received xxxxxx

Accepted for publication xxxxxx

Published xxxxxx

December 2025

Abstract

The MAST Upgrade Super-X divertor protects plasma-facing components from heat fluxes during steady-state operation and transient events. This paper examines heat loads from sawtooth events with energies of $\Delta W_{\text{sawtooth}} \approx 2$–$9\,\text{kJ}$ in lower single null plasmas. The impact of deuterium and nitrogen gas pressures on mitigating these transients is investigated. In the D_2 gas scan for transients with energies up to $\Delta W_{\text{sawtooth}} = 6$ kJ, peak heat flux is proportional to transient energy and inversely proproportional to neutral pressure. Together, the variation in transient energy and deuterium gas pressure accounts for 70% of the variation in peak heat fluxes at the target as measured by infrared thermography and 79% of the "Burn Through Factor" as inferred by D_2 Fulcher band spectroscopy.

Larger sawtooth transients ($\Delta W_{\text{sawtooth}} \approx 6$–$9\,\text{kJ}$) fall outside this trend and shows much higher heat fluxes even at the highest deuterium pressures. A comparison across a range of deuterium pressures shows significantly lower peak heat fluxes for similar transient energies in the Super-X compared to conventional divertor configurations. This reduction in heat flux is consistent with, but not significantly exceeding, expectations based on geometry.

Nitrogen gas seeding was applied to transients with energies below $\Delta W_{\text{sawtooth}} \approx 6$ kJ. Increasing the nitrogen pressure yields a very large reduction in peak heat flux, about 4.5 MW/m^2/Pa, leading to complete buffering of sawtooth transients at higher nitrogen pressures. Direct divertor electron temperature and density profiles were obtained from Thomson scattering mesaurements during transients along a chord running from the target to 0.4m poloidally from the target, aligned along the separatrix. These indicate quiescent inter-transient temperatures of <1 eV, corresponding to strong detachment. The temperatures rise to 6–8 eV during sawtooth transients, with profiles showing decreasing T_e and increasing n_e toward the target. In cases where divertor heat loads exceed $q_\perp > 2$ MW/m^2, we observe T_e along this chord exceeding 10 eV.

The experimental data on transient heat flux mitigation and profiles obtained are compared to modelling results using a 1D exhaust code in the *ReMKiT1D* framework. The modelling showed an increase in heat load for transients with energy $> 4-6kJ$, which is qualitatively similar to the rapid increase in heatload observed for experimental transients with energies $> 6kJ$. Similar temperature and density profiles to those obtained in experiment were predicted. The modelling has shown the importance of recycling due to adsorption and desorption at the target. Delaying recycling to 1ms after the transient event, that is a 1 ms wall neutral *retention time*, is found to match well with experimental data.

Keywords: Buffering, Burn-through, Ultrafast Spectroscopy, Divertor Thomson Scattering, Transients, Reattachment, Sawteeth, Super-X

1 Introduction

The reliable handling of transient heat loads remains a key challenge for the next generation of magnetically confined fusion devices. Plasma instabilities such as sawtooth crashes and edge localized modes (ELMs) release stored thermal energy, delivering intense bursts of heat flux to plasma-facing components (PFCs) [1, 2]. In reactor-scale devices, the current thinking is that large transient heat loads such as those due to type I ELMs will have to be completely prevented, as transients of this size would damage divertor targets reducing machine lifetime [3–5]. However, studying transients is important, because not all transients can be prevented (for example H-L back transitions or sudden release of energy due to impurity ingress) and also because if certain transients can be tolerated it can open up the possibility to operate in different regimes. For example, if operation with transients of $\Delta W = 0.1\%$ is permissible on future machines, this may make a regime with very small grassy ELMs or similar possible.

The MAST Upgrade (MAST-U) experiment was designed, amongst other things, to explore advanced divertor configurations, in particular the Super-X divertor (SXD) [6, 7]. By extending the outer divertor leg, increasing flux expansion at the target and increasing the connection length, the SXD reduces $T_{e,target}$ and reduces heat and particle flux at the target by spreading it over a larger area[8][9][10]. These geometry improvements allow for easier detachment and mitigate both steady-state and transient power loads. Additionally, the Super-X configuration allows a high neutral pressure in the divertor which increases exhaust power dissipation before the strike point [11, 12]. Taking all these factors into account, the Super-X then provides a potential power handling solution for future fusion power plants [13], albeit at higher implementation cost due to the additional coils and infrastructure required.

For STEP, the maximum allowable long term heat load is 10 MW/m^2 and 20MW/m^2 for transient heat loads[14], which are similar to the ITER requirements [15]. For context, experiments have been performed [16] on bulk tungsten showing it can withstand 300 MW/m^2 for 1ms but this decreases with repetitive cycling.

ELM transients have been a particular focus of concern and their impact on machine survivability has been an active area of research [17, 18]. A recent paper on transient heat loads on MAST-U focused specifically on ELMs [19]; this current paper extends this analysis to sawteeth. Sawtooth crashes in MAST-U typically release energies on the order of a few kilojoules [20] similar to the energy loss in ELM events. Although the per transient sawtooth energy loss is small in absolute terms compared to reactor scale tokamaks, these experiments provide an important test case for assessing transient heat load mitigation strategies.

In this paper, we investigate the mitigation of sawtooth-induced transient heat loads in the MAST-U Super-X divertor configuration. We present experimental measurements of how deuterium and nitrogen gas pressure affect peak divertor heat flux, analyze the scaling with transient energy, and compare the transient heat flux mitigation performance of Super-X and conventional divertor configurations. Impurity seeding with nitrogen has been used to increase radiative power dissipation, and thereby reduce peak target heat flux [21][22].

Section 2 describes the experimental set up and key diagnostics utilised in this work. Section 3 presents results from a deuterium gas scan showing the impact of neutral deuterium pressure in the divertor on sawtooth burn through. Section 4 examines *high burn through events* (HBEs) where $\Delta W > 6kJ$ which cause proportionally much greater target heat flux than the lower energy transients. For the purposes of this paper, we define burn-through as cases in detached divertor scenarios in which the transient energy is insufficiently buffered and the plasma reattaches to the divertor target tiles. We consider that the plasma is attached if the ionisation region is attached to the divertor target, which in our data corresponds to a plasma temperature >1 eV within a distance 10 cm poloidally from the target. Section 5 compares transient heat loads in Super-X and conventional configurations. Section 6 looks at a nitrogen gas scan, which is shown to mitigate the heat loads effectively for the transient energy range studied. Section 7 shows direct measurements of temperature and density profiles near the target ($T_{e,div}$ and $n_{e,div}$) and relates these to heat flux measurements ($q_\perp$). Section 8 shows modelling results from the ReMKiT1D framework which reproduces many of the experimental results and thus faciliates understanding of the underlying physics.

Table 1: Diagnostics used in this study and their time resolution.

Diagnostic	**Integration Time** [μs]
Ultra Fast Divertor Spectroscopy (UFDS)	10
Divertor Thomson Scattering (DTS)	0.01
IR Camera (IR)	295
Fission Chamber	100
Fast Ion Gauge (FIG)	10,000
Equilibrium Reconstruction (EFIT)	600

2 Experimental Setup and Diagnostics

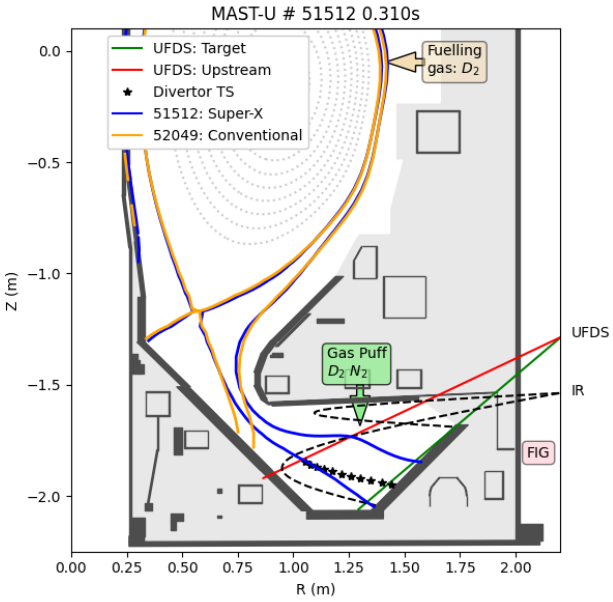

Figure 1: MAST-U geometry showing the last closed flux surfaces for Super-X and conventional divertor discharges, both in lower single null configuration. Location and lines of sight of key diagnostics used in this paper are overlaid, IR: Infra-Red Camera, FIG: Fast Ion Guage and UFDS: Ultra Fast Divertor Spectroscopy. Also shown are the divertor and main chamber gas valves used in this experiment.

Experiments were conducted on the MAST Upgrade (MAST-U) spherical tokamak [6], which is equipped with the Super-X divertor (SXD) [7]. The SXD features extended outer divertor legs and a large major radius target location, increasing magnetic connection length and flux expansion to mitigate divertor heat loads. For comparison, a subset of discharges was performed in the conventional single-null divertor (CD) configuration under matched plasma conditions. The results of the data from the outer strike leg are examined in this paper, the less well diagnosed inner strike leg, which is not in Super-X configuration, are not investigated.

The plasma scenarios analyzed consisted of lower single null, L-mode plasmas with plasma currents of $I_p \approx 0.75$ MA and toroidal magnetic fields $B_T \approx 0.6$ T on axis. Sawtooth instabilities[20] were naturally present in these discharges, releasing transient energies in the range $\Delta W_{\mathrm{sawtooth}} \approx 2$–$9$ kJ. In all cases, the energy loss over the transient, $\Delta W_{\mathrm{sawtooth}}$, was determined from core magnetic diagnostic data which has been used in equilibrium reconstruction [23]. The plasmas had a single neutral beam injecting at the vacuum vessel midplane only (z=0 m) with typical injected heating power $P_{NBI} = 1.6$ MW and did not deploy the *off-axis* beam which injects 65 cm above the midplane. All discharges studied as part of this work were in L-mode, which was ensured by application of low field side rather than high field side gas fuelling [24]. This is important as the transient heat fluxes considered in this paper are then from sawteeth only and not from sawtooth driven ELMs. Lower single null plasmas were chosen in preference over double null plasmas as this doubles the heat flux to the lower divertor.

To study the effect of divertor pressure and impurity seeding on transient heat flux buffering, systematic scans of deuterium and nitrogen gas injection rates were performed. These scans were performed from a divertor gas nozzle and with cryoplant off. While the divertor gas was varied, the low field side main chamber fuelling gas was constant for all discharges. Gas was puffed from dedicated divertor gas nozzle at rates sufficient to bring divertor neutral pressures up to ≈5 Pa in deuterium only plasmas and up to ≈0.3 Pa in nitrogen seeded plasmas.

One of the key diagnostics for this work is the Ultra-fast divertor spectroscopy (UFDS) which provided measurements of divertor plasma conditions from filtered visible spectroscopy. The principle filter used was the Fulcher band measuring D_2 molecular emission with central wavelength 600 nm and full width half maximum of 10 nm. The edge of the peak intensity of the Fulcher emission we take to be the ionization front location[11].

This current work on Sawtooth transients in lower single null discharges was preceeded by a related study of transient heat loads as a result of ELMs in double null discharges [19]. The previous work [19] showed the de-

gree to which ELM transients with energies $>\approx 2-3$ kJ burn through the detachment front depends on neutral pressure, see in particular figure 7(e) of that paper. For that paper, burn through was inferred as being the point where Fulcher emission at the target was similar to Fulcher emission 0.4m poloidally upstream from the target. This current work uses some of the methodology which has been developed for that previous study and is explained in that paper. As well as the different physics aspects, there are some key diagnostic differences. The previous work exclusively used the spectroscopic measurement to infer burn through as no fast infra-red camera data was available during that campaign. This current work makes extensive use of the infra-red camera data which is operated at 295μs resolution allowing good diagnosis during transient events. The target/upstream ratio from Fulcher spectroscopy corresponds well with the peak target heat flux from IR measurements. Although the infra-red camera $q_{\perp}$ is a direct measurement of heat flux compared with spectroscopy measurements, UFDS offers much better time resolution at 10μs. Since the previous work, the UFDS diagnostic has been upgraded from 5 to 10 lines of sight offering greater spatial resolution. The layout of the various diagnostics and the equilibria of the lower single null plasmas are shown in figure 1. This new paper uses the DART code (**D**etachment **A**nalysis with **R**educed modelling **T**ools)[1], [14], while the previous work relied on direct measurement of pressure from the Fast Ion Guage (FIG) in the sub-divertor. The DART value is used in this paper in preference to the FIG measurement as it provides the average pressure in the divertor chamber which is more local to the point of interest and also, the FIG data saturates at values above 1Pa. Note FIG measures the neutral gas pressure at a fast rate and does not relate to fast ion pressure.

Divertor heat fluxes were measured by an infrared (IR) thermography system viewing the outer target[25]. The IR data were analyzed using a surface heat transport code to infer the perpendicular heat flux profiles during and between sawtooth crashes.

Divertor Thomson scattering [26–28] provides local measurements of electron temperature ($T_{e,div}$) and density ($n_{e,div}$), at 10 locations over a 0.4 m chord poloidally from the target at a repetition rate of 30 Hz. The location of measurement points for the divertor Thomson are shown in figure 1. The integration time for DTS measurements is the laser duration of 10ns, which is effectively instantaneous with respect to the transient timescales considered in this paper. A summary of the various diagnostics used in this paper and their time resolutions is provided in table 1.

3 Deuterium gas scan

Deuterium gas injection into the divertor chamber was varied from 0 to 1.2×10^{22} particles/s over the eight discharges shown in Figure 2. The midplane gas puff was held constant at 0.45×10^{22} particles/s during these periods. Both the measured sub-divertor and inferred divertor chamber pressures are plotted in the first column of Figure 2. For the discharges shown here, the FIG measurements saturate at ≈1Pa. The next two columns of Figure 2 show the neutron flux measured by the fission chamber [29] and the plasma stored energy estimated by EFIT [23], which was run at a fast time resolution of 600μs. Both sets of traces show clear signatures of sawtooth events characteristic of this scenario. The sawteeth show some variation in amplitude both across discharges and within each discharge, in particular there are some larger sawteeth intermittently later in certain discharges. Other than the divertor gas pressure no other parameters were changed within the discharges. The fission chamber data exhibit low noise, whereas the EFIT energy trace shows more visible fluctuations. Previous work [19] estimated an uncertainty of approximately ±0.9kJ in the determined ELM energy loss ΔW_{ELM} from EFIT and a similar level of uncertainty is expected for estimating sawtooth transient energy losses $\Delta W_{\mathrm{sawtooth}}$. Additionally, due to the toroidal asymmetry of the internal kink associated with sawteeth, the EFIT energy trace shows 'spikes' and 'troughs' immediately before the crash. The sawtooth transient energy loss was determined by fitting the EFIT energy evolution linearly before and after each event and evaluating the difference at the sawtooth crash time, which itself was identified from the corresponding drop in neutron flux.

The penultimate column of figure 2 shows the ratio of Fulcher band emission between the viewing chord closest to the divertor target and the most upstream chord, as depicted in Figure 1. As discussed in [19], this ratio increases sharply during transients energy releases, reflecting the movement of high temperature plasma along the field lines towards the target. More emission at the target than upstream, $T/U > 1$, is used as an indicator of detachment front position. Finally, the last column of figure 2 presents the peak heat flux measured on the divertor target tile by the infrared (IR) thermography system. The heat flux is plotted on a scale from 0 to 2MW/m^2, which encompasses the majority of transients; the relatively few transients exceeding this range will be discussed in section 4.

Within the discharges of the deuterium gas pressure scan, it is observed that generally as the gas flow rate is increased, both the Target/Upstream Fulcher ratio and the peak IR-measured transient heat flux typically de-

[1]DART can be accessed through: https://git.ccfe.ac.uk:shenders/dart.)

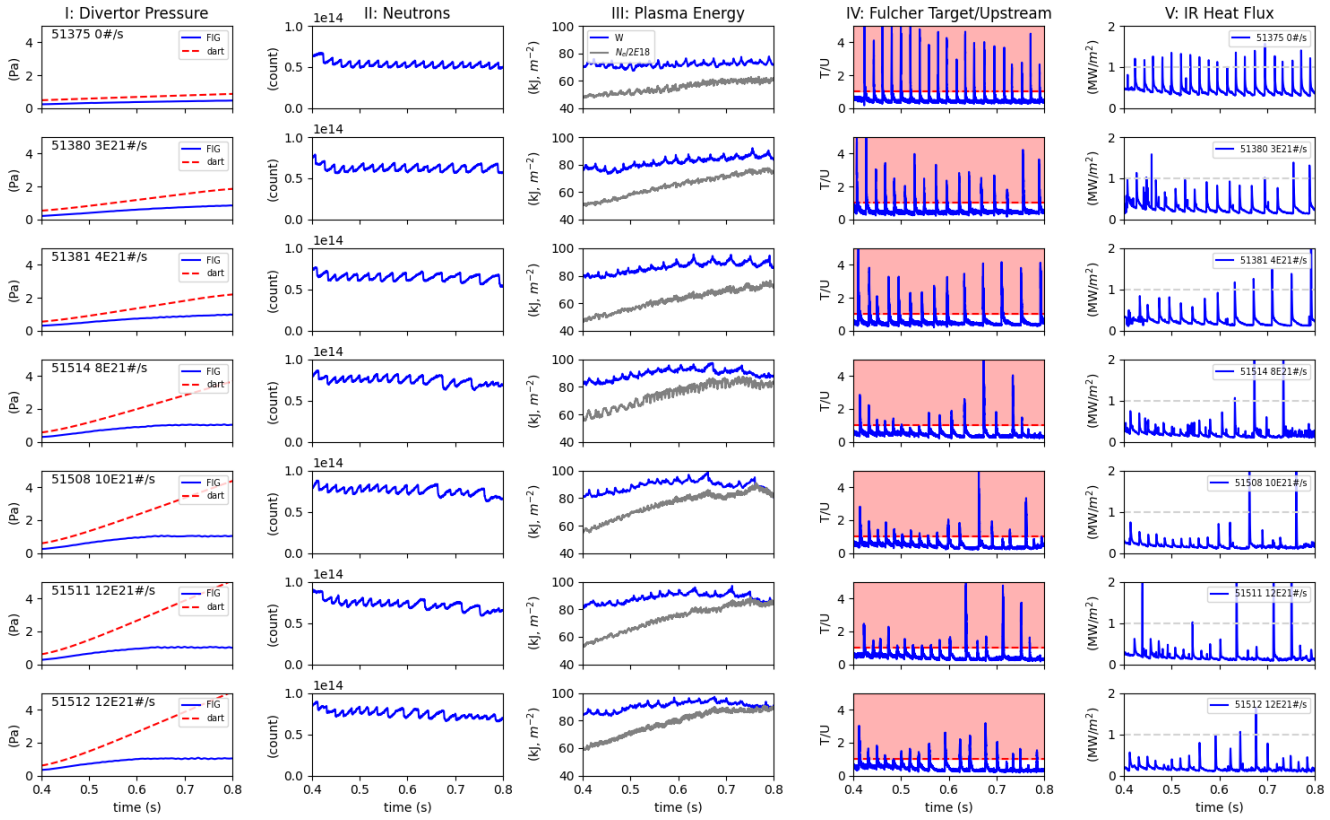

Figure 2: Overview of sawtooth mitigation experiment during the deuterium gas pressure scan. First column: measured sub-divertor gas pressure (fast ion gauge) and inferred main divertor chamber pressure (from DART). Second column: neutron flux measured by the fission chamber [29]. Third column: plasma stored energy from EFIT reconstructions [23], with visible sawtooth crashes. Line integral density (gray) overlaid for reference. Fourth column: ratio of Fulcher band emission between the viewing chord near the divertor target and the upstream chord Fifth column: peak divertor target heat flux measured by IR thermography.

creased. This behaviour indicates that raising the divertor deuterium gas pressure can effectively reduce the peak heat loads from sawtooth transients in this energy range, consistent with spectroscopic observations previously reported for ELM transient mitigation [19].

The individual sawtooth transients identified in the discharges shown in Figure 2 were analysed and compiled into a database, recording both the transient energy loss and the corresponding divertor neutral gas pressure for each event. In total, 138 sawtooth events were analysed; of these, 130 are low burn through events $q_{\perp,max} < 2\mathrm{MW/m}^2$ and are presented in Figure 3, the eight high burn through events $q_{\perp,max} > 2\mathrm{MW/m}^2$ are examined in the following section of this paper. The top row of Figure 3 shows the Fulcher Target/Upstream emission ratio plotted against: (a) the divertor main chamber neutral pressure inferred from DART, (b) the transient energy loss ΔW, and (c) the ratio ΔW/Pressure. The bottom row presents the peak infrared (IR) heat flux observed on the divertor target during each transient, plotted against the same three parameters. The integral heat flux widths in this dataset are in the range 0.11-0.14m.

As shown in figure 3(a), the Target/Upstream Fulcher ratio decreases significantly with increasing neutral gas pressure. Similarly, Figure 3(d) indicates that the peak IR heat flux also decreases with higher neutral gas pressure. Together, these results suggest that increasing divertor deuterium gas pressure mitigates burn-through and peak heat loads during sawtooth transients of these energies. The dashed lines in figs 3 (a) and (d) show a fit scaling the T/U value and $q_{\perp,max}$ with the reciprocal of neutral pressure and this fit appears to be a reasonable fit to the data.

Figures 3(b) and (e) show that both the Target/Upstream Fulcher ratio and the peak IR heat flux increase with the magnitude of the transient energy loss ΔW. To investigate whether the variation in burn-through can be largely attributed to these two variables, transient energy and neutral gas pressure, figures 3(c) and (f) plot the burn-through indicators against the combined parameter ΔW/Pressure. Within this dataset, this combined parameter explains 79% of the observed variation in the Target/Upstream Fulcher ratio and 70% of the observed variation in $q_{\perp,max}$, indicating that transient energy and neutral pressure together largely govern the divertor response to sawtooth events. The increase in Target/Upstream ratio increasing with ΔW/Pressure implies more high temperature plasma at the target and more recycling at the target.

Comparing burn through versus transient energy and neutral pressure is motivated by the model for ELM burn-through [19], where it was found that whether or not an ELM burns through is well described by these two parameters. The results from this sawtooth dataset indicates increasing heat flux depending on ΔW/Pressure.

4 High Burn Through Events

Three of the eight discharges from the deuterium gas scan are shown in figure 4. These three discharges were selected as they contain 7 of the 8 transients where $q_{\perp,max}$ exceeds $2MW/m^2$. It is not understood why these particular discharges give rise to individual sawteeth with larger heatfluxes, other than the divertor chamber gas puff all eight discharges are identical. The first row shows the drop in neutron flux which is indicative of the sawtooth amplitude. The second row shows the absolute signal level observed from the target line of sight of the UFDS. For this plot we use the absolute signal level, rather than the target/upstream ratio, as absolute signal level is more directly related of the magnitude of the transient. The final row shows the peak IR heat flux at the target, with a maximum y scale of $8MW/m^2$ in comparison with the maximum y scale of $2MW/m^2$ used in figure 2.

From the neutron flux trace, it is evident that some sawteeth have a longer inter-transient time and these sawteeth then show larger drops at the sawtooth time. Observations from the spectrograms show no significant difference in MHD behaviour between the large and regular amplitude sawteeth. Thomson scattering profiles across the sawtooth show evidence of larger amplitude drop in the core electron temperature in the larger sawteeth, but qualitatively very similar behaviour. Infra-red camera data show although there is a larger peak power flux during the larger sawteeth, the duration and spatial extent of heat flux to the divertor are similar. Hence, these larger events, which we will term *High Burn Through Events* appear to be larger sawteeth but not qualitatively different. These *High Burn Through Events* are interspersed with the lower amplitude sawteeth, so do not appear to be driven by some global evolution in the core plasma behaviour such as current profile evolution.

The Fulcher target intensity and IR peak power loads show that these *High Burn Through Events*, despite being only slightly larger in terms of neutron loss and by inference ΔW, are proportionately much larger in terms of impact on the divertor. This implies that these larger events are in a different divertor physics regime compared to the lower amplitude sawteeth.

The sawtooth dataset is analysed on a per transient basis and the results are shown in figure 5. To illustrate the difference between *High Burn Through Events* and smaller sawteeth, the two are displayed separately differentiated by peak target heat load.

Figure 5 shows that the $> 2MW/m^2$ events exhibit very little relation to the trends that were determined from the $< 2MW/m^2$ dataset. Figures 5(a) and (b) shows that

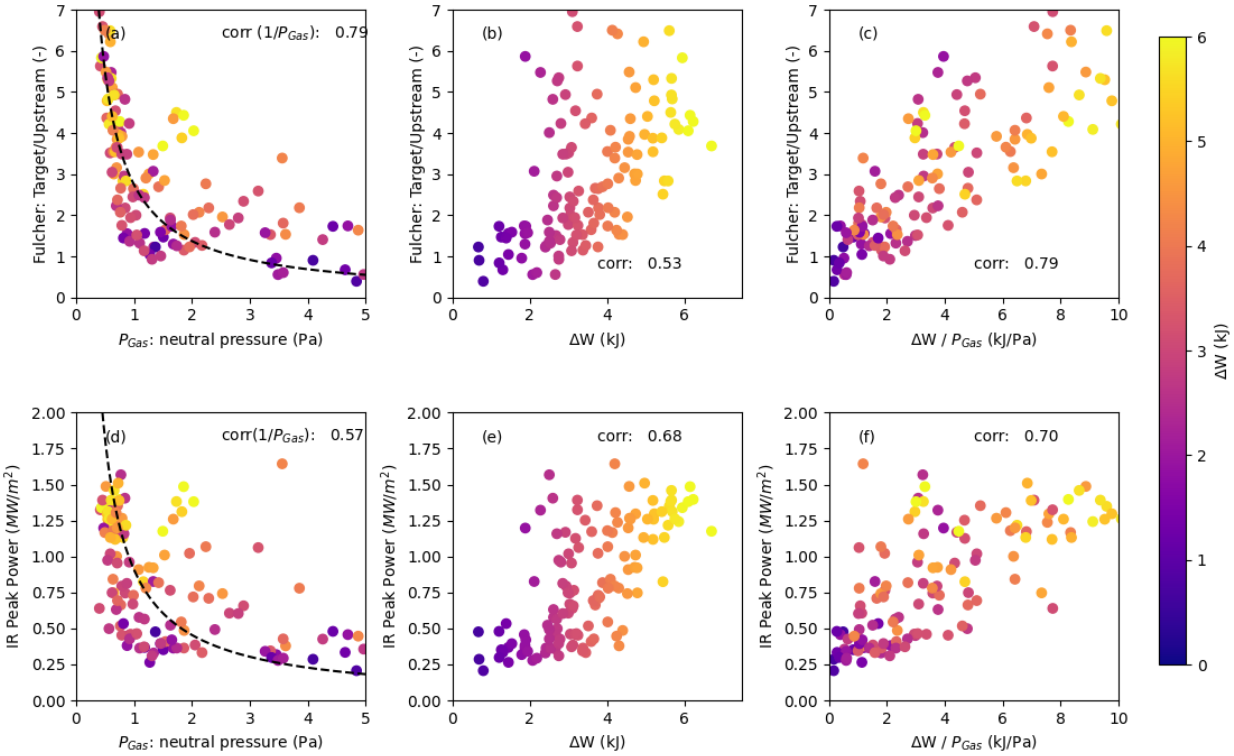

Figure 3: Statistical analysis of 130 sawtooth transient events with $q_\perp < 2\text{MW/m}^2$. Top row (a–c): Fulcher Target/Upstream emission ratio plotted versus (a) main divertor neutral gas pressure, (b) transient energy loss ΔW, and (c) combined parameter ΔW/Pressure. Bottom row (d–f): peak IR-measured divertor heat flux during transients plotted versus the same parameters.

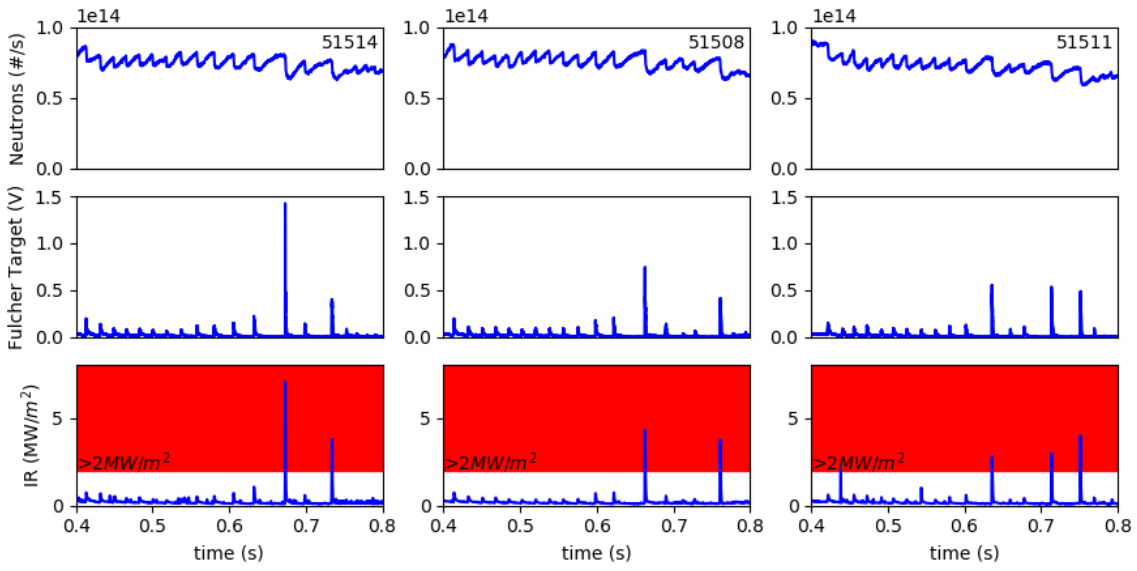

Figure 4: Three representative discharges from the deuterium gas scan illustrating *High Burn Through Events* (HBEs). First row: neutron flux measured by the fission chamber, showing larger sawtooth crashes as deeper drops in neutron emission. Second row: intensity of Fulcher band emission from the divertor target view (UFDS diagnostic). Third row: peak divertor target heat flux measured by the IR camera, plotted on a higher scale (0–8 MW/m^2) than Figure 2 to highlight larger transients.

the *High Burn Through Events* are all higher higher ΔW and neutron loss events. From figure 5(c) the HBEs are happening at low $\Delta W/P_{gas}$ which contradicts the trend from the $< 2MW/m^2$ dataset shown with a linear fit for illustative purposes. The expected uncertainty in measured transient ΔW of ± 0.9 kJ, is shown in figure 5(a), given this uncertainty it is likely that there is an energy above which *High Burn Through Events* occur, the neutron losses per event are shown as these have very low statistical uncertainty in contrast to the energy loss measurement. Figure 5(d) shows the sawtooth duration versus the sawtooth size, as measured by the drop in neutron rate, this confirms that the larger sawteeth (and hence HBEs) correlate with longer inter sawtooth times.

While for the lower burn through dataset ($< 2MW/m^2$), it was shown that increasing the deuterium pressure resulted in lower target heat loads and reduced burn-through, it is not clear for the HBEs that deuterium pressure is a significant factor. It could be that the HBEs deliver sufficient energy to locally re-ionise the divertor neutrals and establish a higher electron temperature at the target. This could lead to disproportionately higher peak heat fluxes despite only modest increases in transient energy loss. Direct measurements of temperature at the target in the next sections test this hypothesis. The presence of HBEs interspersed with smaller events within the same discharge indicates that the transition to this regime is sensitive to the magnitude of the transient and is not governed by slower changes in background plasma conditions.

5 Comparison of Conventional and Super-X Divertor Transients

Discharge 51512 is a Super-X discharge with divertor gas fuelling at $1.2 \times 10^{22} D_2$/s. Discharge 52049 is a conventional divertor variant of 51512 with identical gas fuelling which was performed to compare transient heat loads between the two divertor configurations. The first column of figure 6 shows that the neutral gas pressure in the divertor chamber is similar between the two configurations, as measured by both the FIG diagnostic and subsequent to this inferred from the DART code. The second column shows the neutron flux, with comparable sawtooth activity in both discharges; an internal reconnection event (IRE) early in the Super-X pulse causes a large drop, but does not affect the later transient behaviour. The third column shows the peak target heat flux measured at the conventional outer divertor target (tile T2) and the Super-X target (tile T5). As expected, the conventional divertor shows substantially higher heat flux both during sawtooth transients and in the quiescent period between transients.

The Super-X divertor is designed to provide improved

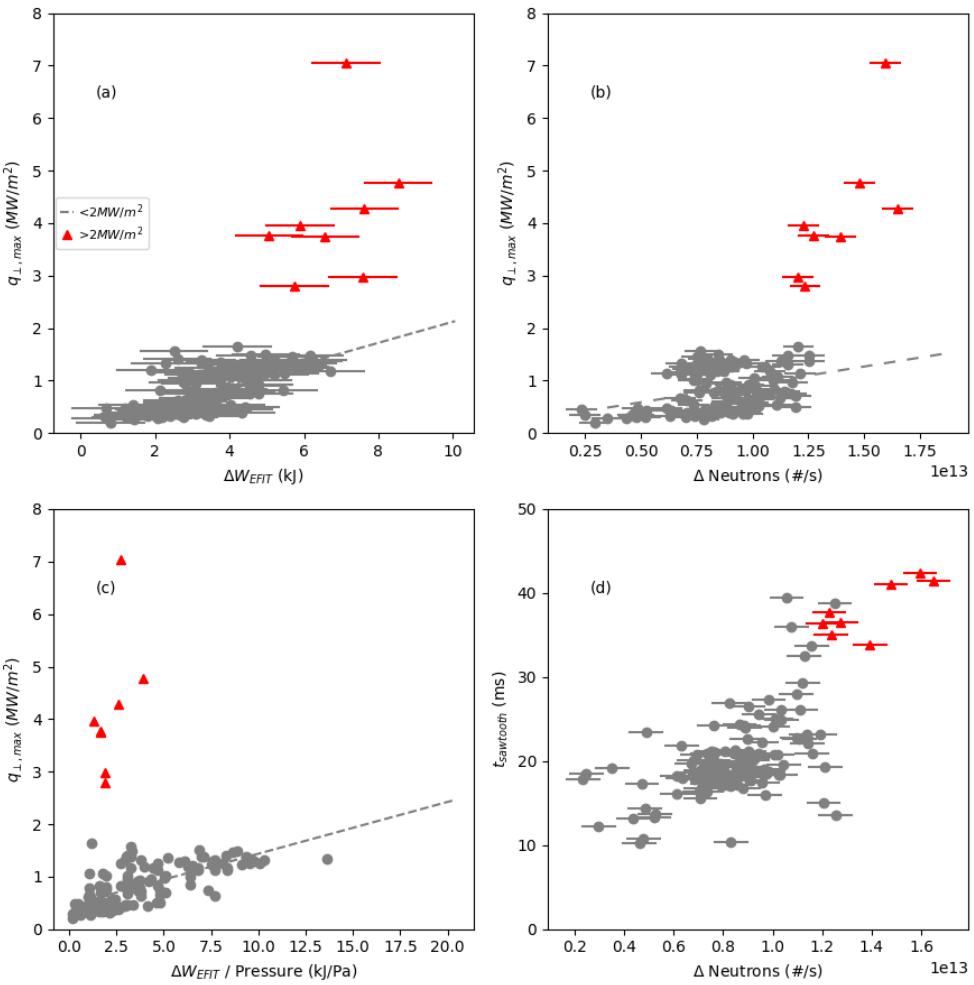

Figure 5: Analysis of individual sawtooth transients, separating *High Burn Through Events* (HBEs) from smaller events. (a) Peak heat flux vs. per transient EFIT energy loss showing errorbars on EFIT energy loss estimation. (b) Peak heat flux vs. per transient neutron loss (the neutron loss is taken to be a proxy for the energy loss, but with lower uncertainty); HBEs correspond to higher energy crashes. (c) Peak heat flux vs. transient energy divided by divertor neutral pressure; HBEs occur across a range of $\Delta W/P_{gas}$ and deviate from the trend found for smaller events. (d) Sawtooth time vs. per transient neutron loss

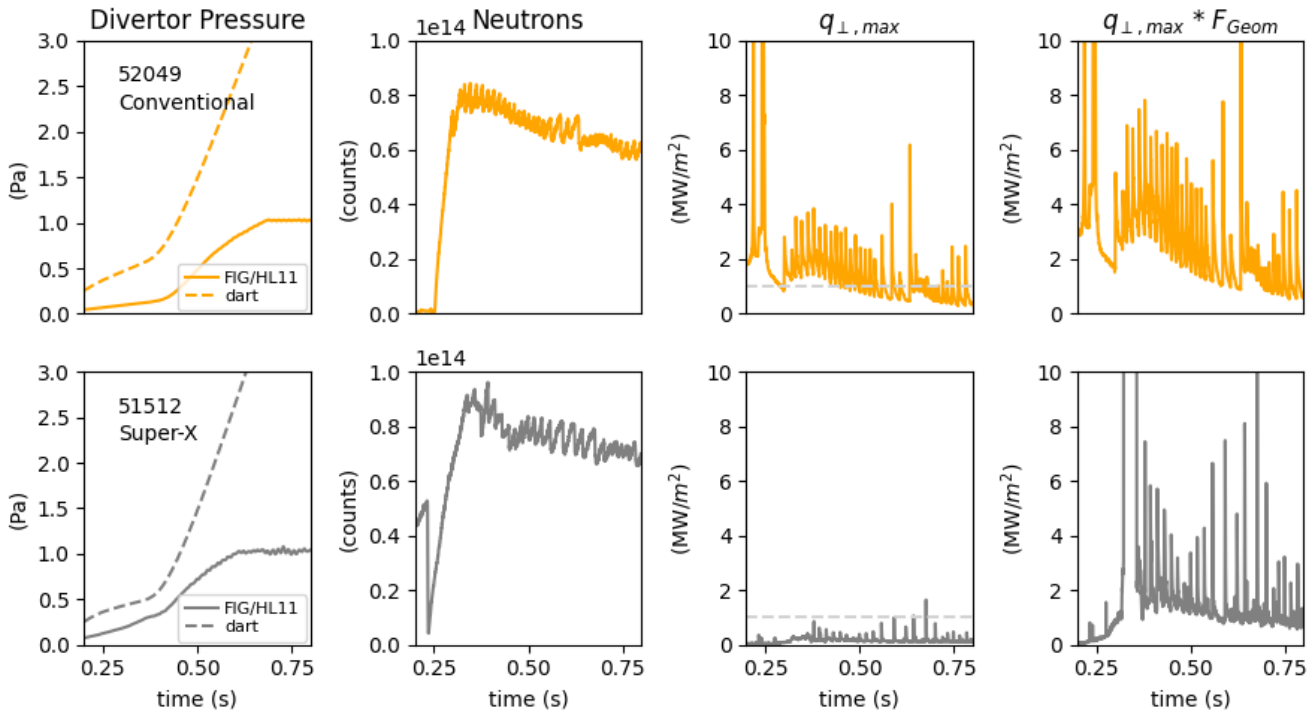

Figure 6: Comparison of target heat fluxes during similar discharges in conventional (top row) and Super-X (bottom row) divertor configurations. Columns show (from left to right): divertor neutral gas pressure; neutron flux from the fission chamber; peak divertor target heat flux measured by the infrared camera; and peak heat flux scaled by the geometry factor described in Eqns. 1–2.

heat flux mitigation compared to the conventional divertor, due both to favourable geometry (increased poloidal and toriodal flux expansion and target tilting) and favourable physics conditions (operation in a higher neutral pressure regime enhancing volumetric power dissipation across a long connection length).

The relationship between heat flux, midplane λ_q and separatrix power during quiescent periods and with energy losses during transient periods can be summarised by:

$$q_{\perp} = \frac{1}{F_{\mathrm{Geom}}} \frac{\Delta W_{transient}}{\Delta t_{transient}} \frac{f_{\mathrm{out}}}{2\pi \lambda_q R_{midplane}} \quad (1)$$

where f_{out} is the fraction of heat flux to the lower outer divertor excluding effects such as radiation and F_{Geom} is a geometry factor that captures the effect of target orientation and magnetic flux expansion. For the MAST-U Super-X configuration, typical values of $f_{out} = 0.5$ and $\lambda_q = 5 - 8mm$[30].

The geometry factor F_{Geom} which is given by the equations below, clearly varies significantly between the Super-X and conventional configurations.

$$F_{\mathrm{Geom}} = f_{\theta} f_{\phi} f_{\theta tilt} f_{\phi tilt} \quad (2)$$

where poloidal flux expansion is:

$$f_{\theta} = \frac{B_{pol-midplane} R_{midplane}}{B_{pol-target} R_{target}} \quad (3)$$

where $B_{pol-midplane}$ and $B_{pol-target}$ are the poloidal magnetic field strength at the midplane and target, respectively. The toroidal flux expansion is:

$$f_{\phi} = \frac{R_{target}}{R_{midplane}} \quad (4)$$

the poloidal tilt effect is:

$$f_{\theta tilt} = \frac{1}{cos(\theta_{poloidal})} \quad (5)$$

where $\theta_{poloidal}$ is the angle between the tile surface-normal vector and magnetic field vector in the poloidal plane. The toroidal tilt effect is:

$$f_{\phi tilt} = \frac{n_r B_r + n_z B_z}{(n_r^2 + n_z^2)^{1/2} (n_r B_r + n_{\phi} B_{\phi} + n_z B_z)} \quad (6)$$

where n_* are the components of the tile surface-normal unit vector. In the case $n_{\phi} = 0$ (no toroidal tilt), $f_{\phi tilt} = 1$

The fourth column of figure 6 plots the IR peak power in conventional and Super-X discharges normalised to the geometry factor. This column shows that for these two comparable discharges, although the absolute level of heat flux is much lower in Super-X, this difference in heat flux is dominated by geometric factors.

Figure 7 presents a transient-by-transient comparison of the conventional divertor discharge shown in figure 6 against all the transients from the 8 discharges of the D_2 gas scan. The figure includes all transients with neutron drops of less than $1.1 \times 10^{13} n/s$, which approximately corresponds to energies $< 6kJ$ and so excludes high burn through events. Figure 7(a) and (b) show the peak heat flux reached during sawtooth events plotted against transient energy and divertor neutral pressure. The data in these figures confirm better transient performance in the super-X than in the conventional configuration. Figure 7(c) shows the geometry factor F_{Geom} as calculated at each transient timeslice from equilibrium reconstruction. Fig. 7(d) normalises peak heat flux by both ΔW and F_{Geom}, showing that the remaining discrepancy between conventional and super-X transient heat load reduces. This suggests that for the case examined, the observed mitigation of transient heat loads in the Super-X divertor are primarily due to the expected geometric effect of equation 2, rather than additional physics differences between the two divertor regimes. The normalised heat flux was binned as a function of gas pressure and the average and standard deviation within each bin used to compare the SXD and conventional divertor performance. Across all four bins the normalised heat flux is better for the SXD case although within error bars, which indicates slightly better divertor heat load performance, beyond geometry in Super-X compared to conventional. This assumes the upstream same λ_q for both conventional and Super-X divertor discharges, which implies λ_q is set by upstream conditions. Although somewhat disappointing, this may well change when impurity gases such as Nitrogen are added to the divertor chamber to cause extra radiation. It is reasonable to expect that this extra radiation would be larger in the super-X than in the conventional regime due to increased path length to the target and neutral and impurity density due to the baffled design of the divertor. The next section addresses the impact of nitrogen on the super-X, but a comparable discharge with nitrogen in conventional divertor has not yet been performed.

6 Nitrogen Gas Scan

A repeat of the Super-X divertor gas scan was carried out with nitrogen fuelling in the divertor chamber instead of deuterium fuelling, as shown in Figure 8. Each discharge had a constant nitrogen flow rate, leading to a rising nitrogen inventory in the divertor over time. The divertor neutral nitrogen pressure was computed using the DART code [31], which can analyse multiple gas species, and is shown in the first column of Figure 8. Peak values of $\approx 0.3Pa$ of N_2 pressure are observed in the divertor chamber. Although no D_2 gas puffing is performed in the

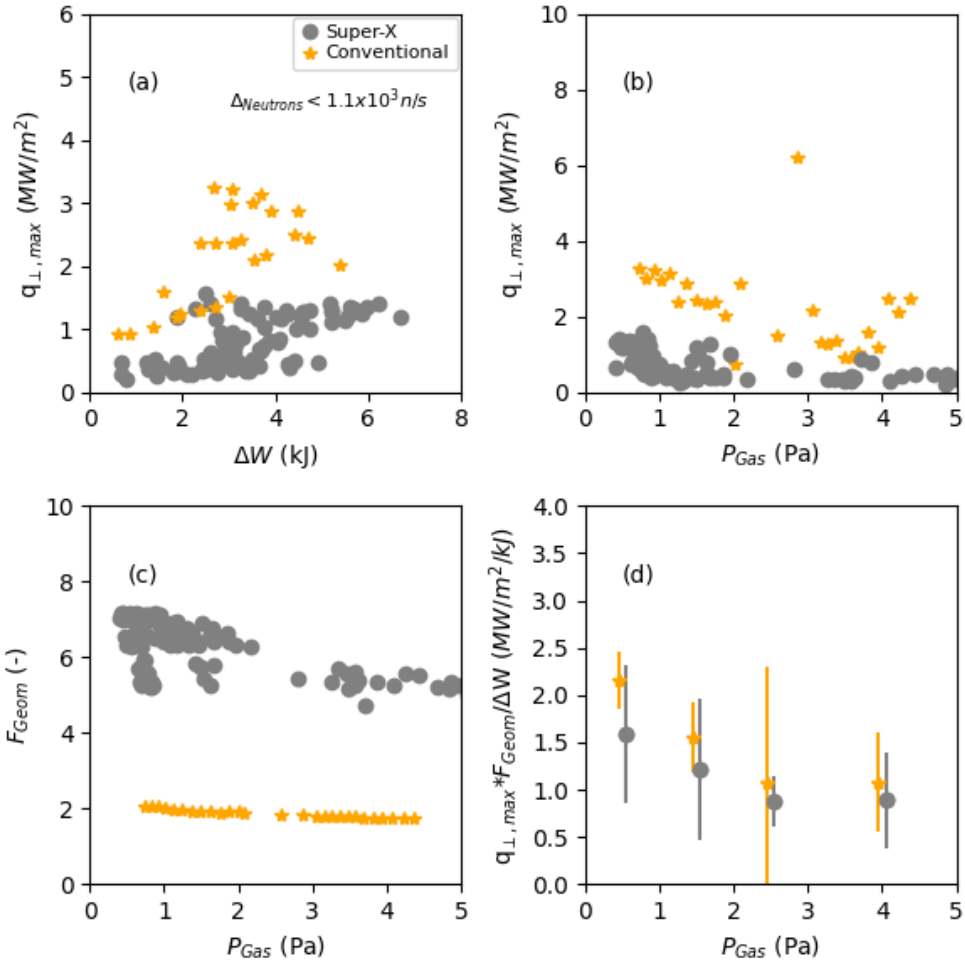

Figure 7: Analysis of individual sawtooth transients comparing conventional divertor discharge (52049) and all the transients from the eight discharges in the deuterium gas scan from figure 2. All plots shown versus divertor neutral gas pressure. (a) Peak target heat flux versus transient energy loss (b) Peak target heat flux versus neutral gas pressure (c) Geometry factor F_{Geom} determined from equilibrium reconstruction [23]. (d) Binned data showing Peak heat flux further normalised by both ΔW and the geometry factor versus transient energy

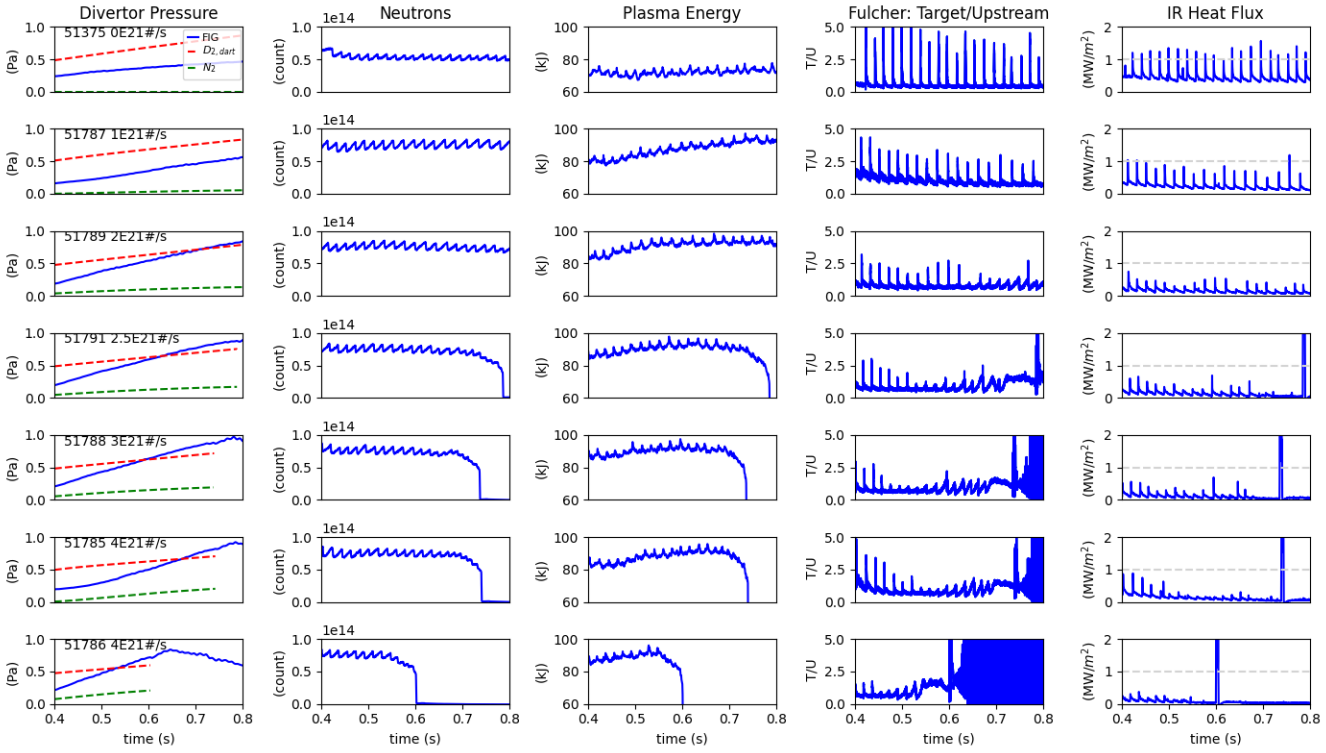

Figure 8: Nitrogen gas scan. Each row corresponds to a single plasma discharge. Columns show divertor D_2 and N_2 neutral pressures calculated from DART, neutron rate, plasma stored energy, target over upstream ratio of Fulcher emission, and peak heat flux from the IR camera, respectively.

divertor chamber during these scans, the D_2 source due to plasma exhaust results in D_2 pressures up to $\approx 1Pa$ at 800 ms.

The amplitudes of the sawteeth, visible in the neutron flux and stored energy (columns 2 and 3), remain relatively uniform within each discharge. However, at sufficiently high nitrogen inventory, radiative cooling leads to plasma disruption, so discharges with higher divertor nitrogen flow terminate earlier. Before disruption occurs, the Fulcher target/upstream ratio and IR heat flux show that nitrogen significantly mitigates the divertor heat flux during sawtooth crashes. For example discharge 51791 which has a flow rate of $2.5 \times 10^{21} N_2/s$ shows Fulcher ratio of $T/U \approx 1$ and IR heat flux of $0.4MW/m^2$, close to quiescent inter-transient levels, versus the unseeded case which has $T/U \approx 4$ in and $q_\perp \approx 1.2MW/m^2$.

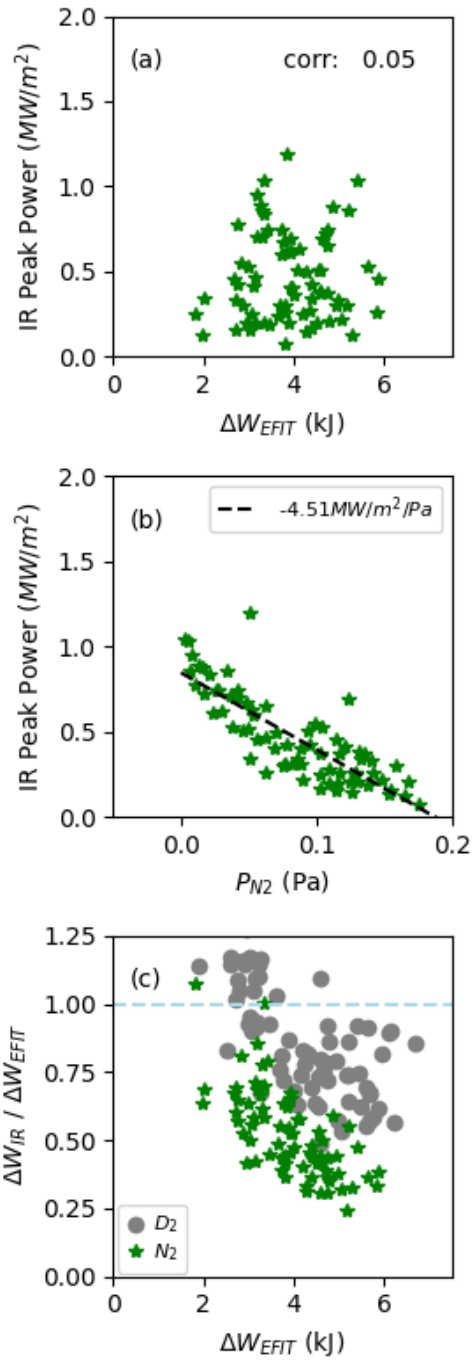

Figure 9: Analysis of the nitrogen gas scan on a per-transient basis. (a) Peak IR heat flux versus transient energy ΔW. (b) Peak IR heat flux versus neutral nitrogen pressure in the divertor. (c) Infra-red camera inferred transient energy loss divided by EFIT energy loss.

Figure 9 shows the per sawtooth analysis of 90 individual transients from the N_2 impurity scan. In contrast to the deuterium gas scan, there is little correlation be-

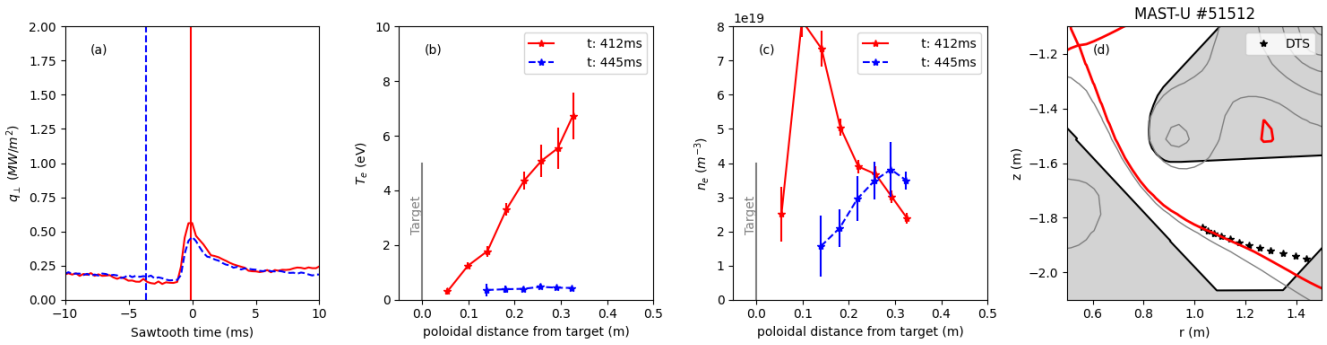

Figure 10: Profiles obtained during a sawtooth event from MAST-U pulse 51512. (a) Peak target heat flux from infra-red camera data relative to transient time. Vertical lines respresent timing of Thomson scattering profiles. (b) Divertor Thomson scattering profiles of electron temperature and (c) electron density near the target. (d) contours of magnetic flux showing the last closed flux surface near the target.

tween the peak heat flux and the transient energy, as shown in figure 9(a). This suggests that, over the parameter space explored, the dominant effect is nitrogen pressure rather than the transient energy. Figure 9(b) shows a steep decrease in peak heat flux with increasing nitrogen pressure estimated at -4.5 MW/Pa. Nitrogen appears to mitigate the heat flux much more effectively than deuterium with 0.3 Pa of nitrogen outperforming 5 Pa of deuterium. Fulcher T/U measurements similarly indicate the strong mitigation of heat flux with 0.3 Pa of nitrogen. This occurs as nitrogen has many atomic emission lines and a low excitation threshold of 2-5 eV thus is well placed to radiate away heat in comparison to deuterium.

No *High Burn Through Events* (HBEs) were observed in the nitrogen dataset (Figure 8). This can be attributed to the lower transient energies ($\Delta W < 6$ kJ) reached in these discharges, as seen in Figure 9(a). The underlying reason why no higher energy events occurred in the N_2 scan compared to the D_2 is less clear. At low divertor pressures, $\approx 0.1Pa$, the main chamber FIG indicates a few mPa of pressure. The main chamber pressure measurement rises to $\approx 10mPa$ at high divertor pressures, where FIG indicates >1 Pa in the divertor chamber. Hence, there may be an indirect stabilising effect of higher deuterium pressure in the main chamber on the sawtooth dynamics, leading to larger transients. Although speculative, this would explain why we don't observe HBEs in the nitrogen scan and why we observe HBEs later in the discharge during the deuterium scans or it may simply relate to random variation in sawtooth energy. Future experiments will examine the impact of nitrogen on $\Delta W > 6kJ$ transients.

The data from figure 9(c) show the energy at the target determined from the IR measurements divided by transient energy loss from equilibrium reconstruction. It demonstrates that there is significant measureable buffering of Transients with Nitrogen impurities in the divertor and that that buffering is much larger than can be achieved with Deuterium gas alone.

7 Divertor T_e and n_e at high heat flux

The divertor Thomson scattering diagnostic was operating over the various gas scans discussed in this paper at its laser repetition rate of 30Hz (33.33ms). The duration of elevated heat flux during transients are ≈1-2ms and the inter-sawtooth time was ≈20ms, so for any given DTS laser pulse there was an $\approx 5-10\%$ probability of diagnosing divertor T_e and n_e during sawtooth. One of the sawteeth diagnosed by DTS is shown in figure 10. A timeslice from the quiescent period before the sawtooth time is overlaid for reference. In figure 10(a) the sawtooth event is indicated by $q_\perp$ and the relative timings of the profiles are shown by vertical lines. For the pulse in the inter-transient period, the temperature is $<\approx 1eV$ (fig 10(b)) and the density shown in (fig 10(c)) falls toward the target. The profiles are typical of a *detached* plasma on MAST-U. UFDS measurements support the indication that this plasma is detached between sawtooth events. The profiles during the sawtooth show elevated temperature up to 8eV at distances 0.4m from the target and density rising toward the target. Based on the peak heat flux at the target at this time, we would conclude that these profiles are indicative of re-attachment albeit at lower T_e than might be expected. This perhaps indicates the distribution is not fully Maxwellian and has a higher content of fast electrons.

No profiles were directly obtained during the 8 HBE sawteeth which were part of the deuterium gas scan. However, making the assumption that the peak heat flux value measured at the target is indicative of the divertor temperature at that time then the data during an IRE

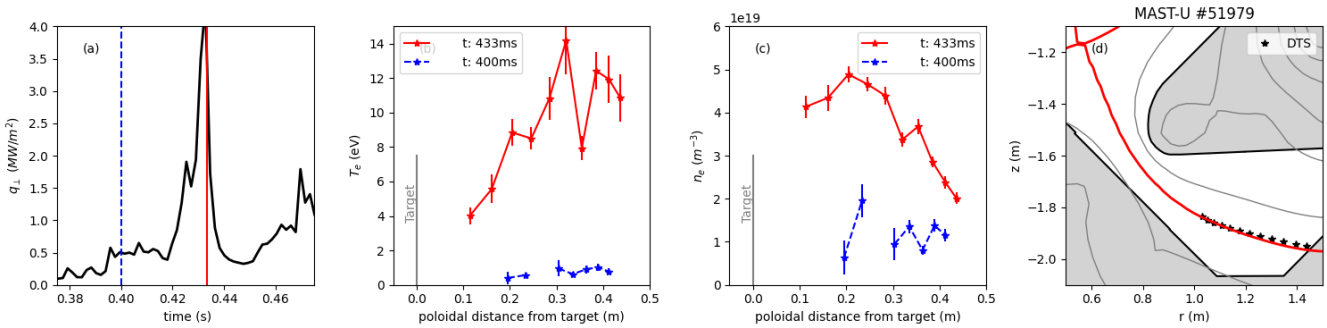

Figure 11: Profiles obtained during a large heat flux event (non-sawtooth) from MAST-U pulse 51979. (a) Peak target heat flux from infra-red camera data as a function of discharge time (b) Measurements from divertor Thomson scattering of electron temperature and (c) electron density near the target. (d) contours magnetic flux showing the last closed flux surface near the target.

which has an energy loss $\Delta W = 15$ kJ is shown in figure 11 provides an indication of what is happening during the HBEs. For further details on IREs on MAST-U see [32] and the references therein. In figure 11, profiles near the target are obtained when the peak heat flux is $4MW/m^2$ with median DTS $T_{e,div}$=8.8eV within 0.4m poloidal distance to the target. This compares with the sawtooth in figure 10 where there is a peak heat flux of $0.6MW/m^2$ and median DTS temperature $T_{e,div}$=4.75eV.

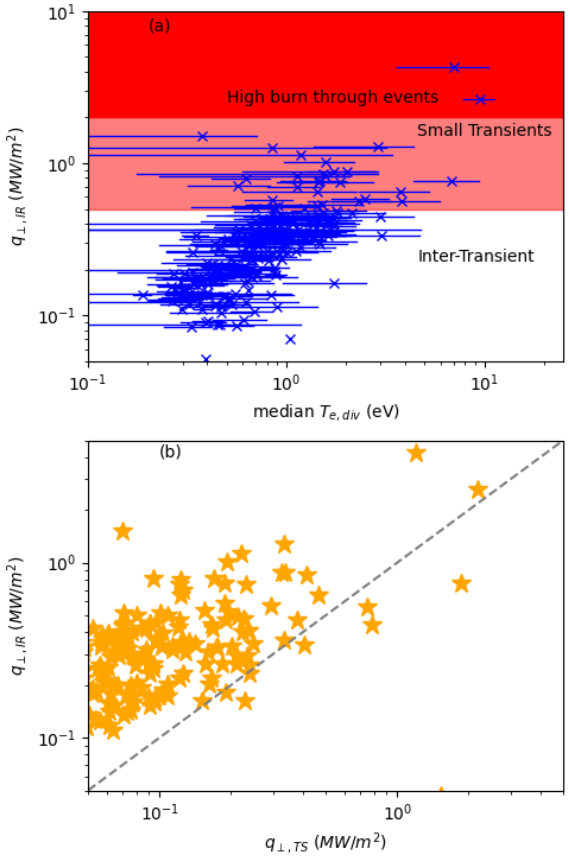

Figure 12: (a) Target heat flux versus median *divertor* electron temperature (as averaged over 0.4m poloidally from the target) from 25 MAST-U discharges (b) IR heat flux versus inferred heat flux from TS obtained temperature and density

To determine more generally the relationship between the peak heat flux in the divertor and the target temperature, data were examined over 25 discharges from

51376-52125, including the N_2 discharges. The only criterion for selection of these 25 discharges was that the strike leg was in the super-X configuration, so in contrast to the data examined elsewhere in this paper, this dataset contains varying plasma current and plasma shaping. Additionally, the data are not limited to discharges with fast IR measurements. The data from this scan are shown in figure 12. For each DTS timeslice, the median value of T_e over the full DTS chord was determined and plotted against the heat flux at that time. The median was used in this case to exclude outliers, which can occur in TS data at very low density. The data show the median divertor temperature increasing with the heat flux from around 0.5eV up to 10eV. For illustative purposes bands are added corresponding to 1) $< 0.5MW/m^2$ which is inter-transient quiescent type heat flux level and typical of $T_{e,div} < 1 - 2eV$ 2) small transients $< 2MW/m^2$ which typically have $T_e < 6 - 8eV$ and result from transient energy losses of $\Delta W <\approx 6kJ$ and 3) HBE type events, including during events such as IREs, which are $> 2MW/m^2$, have $T_e > 8 - 10eV$ and result from transient energy losses of $\Delta W >\approx 6kJ$.

$$q_{\perp,\mathrm{TS}} = \frac{1}{F_{\mathrm{Geom}}}\Big[7\, n_e T_e \sqrt{\frac{2T_e}{m_i}} + 13.6\, n_e \sqrt{\frac{2T_e}{m_i}}\Big] \qquad (7)$$

The data in figure figure 12(b) show the peak heat flux measured from the IR camera compared with the peak heat flux inferred from the median measurements of DTS T_e and n_e along the 0.4m chord poloidally from the target. The inferred heat flux from TS is given by equation 7 which has components for both the surface recombination, where 13.6 eV is the ionisation energy, and the sheath limited heat flux where $\gamma = 7$ is the sheath heat transmission coefficient. The TS inferred heat flux shows reasonable agreement with that measured from IR and in particular the two scale well over the range of heat flux considered.

8 Exhaust Simulations

In order to obtain a better understanding of electron kinetic parameters in the divertor an effort was made to compare the experiment results with expectations based on simulation. In particular the object was to compare the electron temperature and density profiles obtained during transients to those predicted by simulations and to look at the variation of target parameters with transient energy. The latter is inferred indirectly from experiment via the heat flux and UFDS data.

8.1 Reduced 1D multifluid exhaust simulations

Simulations from a multifluid 1D exhaust code written in the ReMKiT1D framework are presented. The code reintroduces many of the features of the SOL-KiT model presented in [33], with the addition of independent fluid equations and variables for ions as in [34], but retaining purely parallel diffusive neutral transport.

Flux expansion is simulated by varying the finite volume cell face area and Jacobian in space. Cells in the upstream 10 m from midplane to x-point are constant area, which then increases linearly by a factor 4 over the downstream 10 m from x-point to the target. Neutral diffusion is also multiplied by a factor 10 to represent field pitch angle enhancement; taking the angle of approximately 84 degrees to the normal of the tile during sawtoothing Super-X shots such as 51518 (Fig.2) Increasing the cell area size (and hence its volume) means there are more neutrals in that volume for a given density. The flux Jacobian gradient roughly approximates that of the inverse magnetic field strength gradient in MAST-U pulse 49197, which is representative of field variation in the super-X configuration but is not intended to be exact.

Global sources and sinks are similar to SOL-KiT: The global energy source is the upstream background heating, 0.8MW to the ions and 0.8MW to the electrons. The plasma sink is the Bohm (narrow sheath) boundary condition applied at the target cell, where 100% of the incident ion flux $\vec{\Gamma}_i$ is converted to neutrals that may be ionised. There are no global plasma particle sources and the total number of electrons, ions and neutrals is conserved. Neutral temperature in this ReMKiT1D model is fixed at the Franck-Condon dissociation temperature of $T_n = 3$ eV, in other words the dissociation of recycled D_2 is assumed to happen on a negligibly short timescale, and no D_2 molecules are present.

Two batches of simulations are conducted to test different **recycling "retention times"** at the wall. Ions reaching the wall are converted to an inert, immobile species (representing wall ad-/desorption) that spontaneously convert to neutral particles after some average time via exponential decay. Here, "instant recycling" refers to a very short average retention time of 10 ns, far shorter than the 1 ms-long transient events of interest. "Delayed recycling" refers to an average retention time of $t_{transient}$, thereby only allowing the release of neutrals from the wall shortly after the transient is deactivated. A consequence of delayed recycling is that there will always be a fraction of the total plasma population that remains wall-embedded, hence the initial plasma inventory must be adjusted for the final equilibria to resemble that of another retention time case.

Each batch consists of a scan across initial plasma in-

ventory to obtain two detached plasma equilibria with identical plasma parameters but different recycling retention times. For each equilibrium, a transient heat flux increase to the background heating power is applied. The "transient" is a fixed increase in heating power of duration $t_{transient} = 1$ ms that is applied either to electrons, ions, or half each to both. A scan of 24 runs per recycling time was performed, including 8 transient energies for each of the 3 lists of transient-heated species.

Considerations were made for the reduced model: The flux tube must be sufficiently heated to realistic core temperatures ($O(10$ eV$)$), whilst cooling to recombination temperatures at the target (< 5 eV). Volumetric energy losses along the flux tube occur solely during electron-ion inelastic collisions, aided by flux expansion. Fixed fraction heavy impurities were used in the past to aid detachment, but are unsuitable for time-dependent simulations of transients in unseeded plasmas. It was not attempted to rigourously tune the input parameters to match the MAST-U observations, but instead use the simplified picture to indicate important physical mechanisms that can apply to a range of shots and parameters.

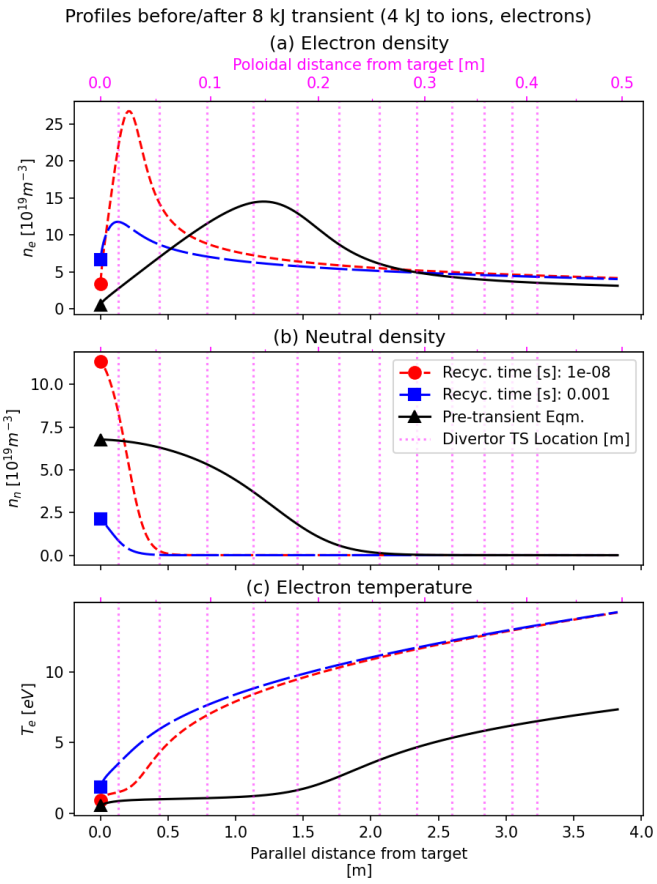

Figure 13: ReMKiT1D simulated profiles of plasma variables versus parallel distance x from the target before and after a 8 kJ, 1 ms heating power transient for two different ion-target recycling retention times. Variables shown in each of the three panels include (a) electron density n_e, (b) neutral deuteron density n_n, and (c) electron temperature T_e. Each panel shows that variable's pre-transient equilibrium (solid black), and the final value of that variable with instantaneous ion-target recycling (short dashed red) and delayed recycling (long dashed blue). Poloidal distances and approximate parallel distances of the DTS/UFDS diagnostic sight lines are shown by dotted pink lines.

8.2 Spatial profiles of plasma parameters

Figures 13(a,b,c) respectively show the electron density n_e, electron temperature T_e and neutral atomic deuterium density n_n versus the parallel distance x from the target (at $x = 0$) in the rest frame of a SOL flux tube. For each plasma variable: the pre-transient equilibrium and end-of-transient profiles are shown for the two recycling retention times.

Also shown in figure 13 on the upper x-axis is the estimated poloidal distance from the target, using reconstructed MAST-U field geometry data depicted by the red curve in Figure 11(d). This represents a known lower Connected Double Null (CDN) Super-X magnetic field geometry that is poloidally aligned with the DTS-UFDS diagnostic sight lines.

The corresponding poloidal distances of each experimental DTS-UFDS diagnostic line of sight are shown by vertical dotted lines. These distance conversions are for rough guidance only in describing the relative sizes of the

plasma phenomena to the diagnostic; there is no poloidal geometry in the ReMKiT1D model, nor will the DTS-UFDS diagnostic lines of sight remain in perfect alignment with the moving flux tube during the transient.

The plasma density n_e profiles are shown in Figure 13(a). The pre-transient detached equilibrium n_e profile initially peaks at a parallel distance of $x = 1.2$ m from the target, or an estimated poloidal distance of 0.15 m. Post-transient, the peak reaches the target while n_e at the target ($x = 0$) is increased. In the instant recycling case, the increased ion flux at the target creates neutrals that are readily ionised, **adding to the electron density already present there and causing an artificial compression**. This feedback loop depletes the plasma of energy once the n_e peak approaches the target, inhibiting further rises in density n_e and electron temperature T_e unless there is a sufficiently high transient energy. Delaying recycling with a rate corresponding with the transient time mostly eliminates this artificial compression while the transient is active. Instead, the n_e peak drops below pre-transient levels and the target n_e increases to 2 times that of the instant recycling case.

For the neutral density n_n in Figure 13(b), the bulk of the initial neutral population pre-transient is burned through in both cases except close to the target, where recycling again determines the outcome. Artificial compression causes n_n at the target in the instant recycling case to increase by nearly 50% rather than decrease by 50% in the delayed recycling case. Because only **heating power transients** are considered, no new particles are added during the transient (to uphold particle conservation in the absence of other sources/sinks). If they were to be included, then the target ion flux would be even higher, enhancing the neutral buildup seen in the instant recycling case than otherwise with a purely heat-based transient.

The electron temperature T_e evolution is shown in Figure 13(c). At pre-transient equilibrium, electron temperature T_e is flat at $\lesssim 1$ eV up to a steep edge that roughly coincides with the n_e peak at $x = 1.2$ m. Post-transient, the T_e edge moves to within 0.3 m parallel distance from the target. In the delayed recycling case, the post-transient temperature increase is greater than the instant recycling case and the T_e floor disappears.

Comparing the end-of-transient n_e profile in Figure 13(a) with the experimental observation in Figure 10(c) a number of observation are made. In both model and experiment, the n_e peak advances closer to the target as the neutrals at the target are ionised during the transient. The n_e peaks become narrower on transient approach to the target and only the downstream edge of the pre-transient n_e peak were captured. The simulated pre-transient peak may be narrower due to the lack of perpendicular neutral transport in the ReMKiT1D model.

Comparing simulated T_e with experiment in Figure 10(b), the measured T_e profile is flat over the full poloidal measurement chord pre-transient whereas in the model the T_e starts to increase at a poloidal distance of 0.2 m from the target. This plasma is known to be detached pre-transient where its front lies further from the target than in the simulated case.

8.3 Scan Data Sampled at Target

48 simulations in total were conducted using the reduced model developed in the ReMKiT1D framework. These comprised 8 transient energies from $1 - 8$ kJ (or $1 - 8$ MW m^{-2} applied for a 1 ms duration). Three different sets of species heated by the transient (electrons only, ions only, and 50% for each), and for the two recycling rates.

Figure 14 shows the line-average value of n_e near the target for each ReMKiT1D run in the full simulation database. The line average of each plasma parameter over parallel distance from midplane $[19.9\text{ m}, 20.0\text{ m}]$ is roughly the poloidal distance between the target and the nearest DTS diagnostic measurement position to the target.

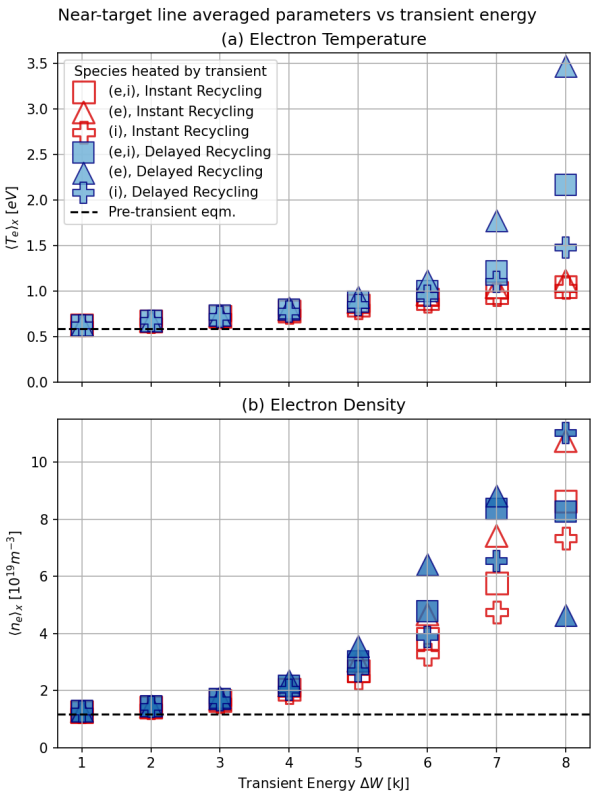

Figure 14: Plasma parameters evaluated adjacent to the target, line-averaged over parallel distance $x = [19.9\text{ m}, 20.0\text{ m}]$, versus transient energy for each list of species heated by transient and each recycling retention time. Marker shape indicates species heated, including 50% transient energy to both ions and electrons (square), electrons only (triangle) and ions only (cross). Marker colour indicates target ion recycling retention time, including instant recycling (red outlined) and delayed recycling (blue filled).

Focusing on electron temperature T_e in Figure 14(a), at lower energies of $\Delta W \lesssim 4$ kJ, both recycling cases gave small post-transient increases in near-target n_e and T_e with weak dependence on which species were heated by the transient. This is due to the plasma not having fully burned through the neutral cloud and reaching the target once the transient ceases. Above $\Delta W \gtrsim 5$ kJ, T_e for the delayed recycling case then increases significantly, particularly in the case of electron only heating. Here, the plasma received enough energy to burn through to the target and is now influenced by recycling. Recalling the profiles in Figure 13, a long recycling wall retention time reduces the neutral population adjacent to the target and the associated plasma energy losses due to collisions, increasing the post-transient T_e there. The effects of recycling at the higher ΔW are dependent on whether the ions or electrons are heated. In this particular model, only electrons carry out ionisations (ion-neutral ionisation is assumed to be negligibly slow) and therefore a transient that heats electrons only will burn through the most neutrals and would produce the greatest T_e increase. Heating ions only will delay the transfer of energy to electrons and subject the energy to additional losses until it is transferred (including the Bohm sheath boundary condition).

For the electron density n_e in Figure 14(b), a similar upward trend in n_e occurs above $\Delta W \gtrsim 5$ kJ, especially in the delayed recycling and electron-heated cases. However, in the delayed recycling case, for the electron-only and electron-ion heating cases, n_e rises then drops beyond $\Delta W \gtrsim 7$ kJ, as the plasma peak advances closer to the target before reattaching and draining into the wall. This is unlike the instant recycling case which has an artificially compressed plasma and neutral density at the target, recalling Figures 13(a,b). A much higher transient energy would therefore be required to deplete the neutrals under instant recycling and prevent further neutral creation through recombination.

Comparing simulation with experiment, the threshold ΔW for the ReMKiT1D model cases is higher, primarily due to the higher plasma and neutral density (more neutrals at target to burn through), but the model also does not include cross-field neutral transport or impurities that would increase the threshold ΔW. In reality, there exists a population of hot, fast electrons with larger mean free paths than the domain. This would mean the collisional fluid electron model described here is likely overestimating T_e in the purely electron-heated case[34–36]. This suggests that if the transient energy and upstream T_e are sufficiently high, this would have less of an effect in increasing the downstream T_e and the ion and neutral physics become more important. Non-local kinetic effects, such as those detailed in [37] and [38], are a primary research question for ReMKiT1D and is subject to future work.

9 Conclusions and Future Work

A divertor D_2 gas scan in the Super-X lower single null divertor configuration has shown significant mitigation of sawtooth transient heat flux by divertor gas pressure where the transient energy ΔW is less than 6 kJ ($\Delta W/W_{plasma} < 7.5\%$). At this energy the transients typically produce peak heat loads below 2 MW/m^2. However, analysis of the full deuterium gas scan dataset reveals a change in target behaviour for transients where $\Delta W > 6$ kJ, suggesting a transition into a different divertor physics regime such as a complete depletion of the transient buffering capability of the divertor.

Recognising that heat loads increase rapidly for larger

transients, it will be necessary in future to explore this higher-energy branch and test mitigation strategies at higher ΔW. Initial attempts to stabilise sawteeth and thereby increase ΔW to test these mitigation strategies were unsuccessful within the available plasma scenario, so alternative methods to access larger transients will be explored in upcoming campaigns.

In the Super-X divertor nitrogen gas scan, N_2 pressure was increased to mitigate transient heatloads which it did very successfully with reduction of $\approx 4.5 MW/m^2/Pa$. However, at high nitrogen pressure disruptions occurred due to radiative collapse. These results suggest the maximum tolerable N_2 pressure before plasma termination. A logical next step is to have a N_2 flow rate which decreases over the course of pulse to sustain a steady high divertor N_2 pressure without triggering disruptions. Such a pulse should maintain effective transient buffering throughout. No data were obtained in the N_2 gas scan from transients with $\Delta W > 6$ kJ. However, the prospect of mitigating these *High Burn Through Events* using N_2 gas remains a promising direction for future investigation.

A comparison of conventional and Super-X divertor configurations with D_2 in the divertor chamber during transient events demonstrated significantly lower target heat loads in the Super-X case. This improvement was largely consistent with expectations from geometric considerations with some indications of benefits beyond geometry alone but at the $<\approx 20\%$ level. A valuable extension would be to repeat this comparison with N_2 seeding in conventional divertor configuration. In this case, the more enclosed geometry of the Super-X divertor may enhance radiative losses and offer improved relative performance.

Profiles of electron temperature and density near the target during transients have been obtained from divertor Thomson scattering showing significant increases in T_e and n_e during the 1-2ms period after transients. A simple 1D fluid exhaust scenario was developed in the ReMKiT1D framework to gain insight into the observed burn-through threshold dynamics. Good agreement in the simulated and observed pre-transient equilibria were seen in the divertor electron density and temperature profiles. In particular, the fall-off of temperature to the target agrees with experiment as well as the peaked electron density close to the target in front of a neutral cloud.

However, the simulated post-transient response is highly buffered by the neutral cloud, requiring a higher transient energy threshold for burn-through than observed. Some initial assumptions held by the 1D reduced code's neutral model would have contributed to the over-buffering, particularly the lack of cross-field transport, the neutrals being fixed-temperature and purely diffusive, and the near-instant ion recycling at the target during a transient. To address some of these assumptions, the recycling timescale was increased to delay neutrals entering the flux tube via recycling, allowing for the plasma to reattach mid-transient. This helped to improve the agreement with experiment in the transient energy threshold, but remains overestimated.

Though beyond the scope of this particular study, ongoing work is aimed at addressing the neutral dynamics challenges in future ReMKiT1D transport models, and also to harmonise with other modelling efforts including SOLPS-ITER. Establishing a benchmark between ReMKiT1D and SOLPS-ITER would then allow for kinetic electron effects to be studied in detail. These effects would likely enhance the degree of detachment in the divertor, thereby increasing the burn-through input energy threshold [35] , but would likely need to be accounted for if extending to future machines.

Good agreement was obtained between the density and temperature profiles obtained from experiment and those from ReMKiT1D modelling, indicating this modelling captures the essential features of the transient behaviour. In particular, the fall-off of divertor electron temperature to the target matches experiment as well as the peaked electron density close to the target in front of an expected neutral cloud. This agreement gives confidence that this modelling could be used going forward to better extrapolate the role of transients on future machines.

Acknowledgements

This work has been part-funded by the EPSRC Energy Programme [grant number EP/W006839/1]. To obtain further information on the data and models underlying this paper please contact PublicationsManager@ukaea.uk. The ReMKiT1D framework respositories are hosted on GitHub: https://github.com/ukaea/ReMKiT1D and https://github.com/ukaea/ReMKiT1D-Python

This work was supported by the Engineering and Physical Sciences Research Council [EP/S022430/1].

References

[1] T. C. Hender and et al., "MHD stability, operational limits and disruptions", Nuclear Fusion **47**, S128–S202 (2007).

[2] A. Loarte and et al., "Characteristics of type I ELM energy and particle losses", Plasma Physics and Controlled Fusion **45**, 1549–1569 (2003).

[3] G. Federici and et al., "Plasma-material interactions in current tokamaks and their implications for next step fusion reactors", Nuclear Fusion **41**, 1967–2137 (2001).

[4] T. Eich and et al., "Scaling of the tokamak near the scrape-off layer H-mode power width", Nuclear Fusion **53**, 093031 (2013).

[5] R. A. Pitts and et al., "A full tungsten divertor for ITER: Physics issues and design status", Journal of Nuclear Materials **438**, S48–S56 (2013).

[6] J. Harrison and et al., "Overview of the MAST Upgrade Super-X divertor", Nuclear Materials and Energy **12**, 1072–1076 (2017).

[7] P. M. Valanju and et al., "Super-X divertors and high power density fusion devices", Physics of Plasmas **16**, 056110 (2009).

[8] I. Katramados, G. Fishpool, M. Fursdon, G. Whitfield, V. Thompson, and H. Meyer, "MAST upgrade closed pumped divertor design and analysis", Fusion Engineering and Design **86**, 1595–1598 (2011).

[9] E. Havlíčková, W. Fundamenski, M. Wischmeier, G. Fishpool, and D. Coster, "Numerical studies of effects associated with the Super-X divertor on target parameters in MAST-U", Journal of Nuclear Materials **438S**, S545–S549 (2013).

[10] A. Fil et al., "Comparison between MAST-U conventional and Super-X configurations through SOLPS-ITER modelling", Nuclear Fusion, Accepted manuscript, 10.1088/1741-4326/ac81d8 (2022).

[11] K. Verhaegh et al., "Spectroscopic investigations of detachment on the MAST Upgrade Super-X divertor", Nuclear Fusion **63**, 016014 (2022).

[12] J. R. Harrison, "Overview of physics results from MAST upgrade towards core-pedestal-exhaust integration", Nuclear Fusion **64**, 112017 (2024).

[13] G. Federici and et al., "An overview of the EU DEMO power plant concept", Fusion Engineering and Design **89**, 882–889 (2014).

[14] S. S. Henderson et al., "An overview of the STEP divertor design and the simple models driving the plasma exhaust scenario", Nuclear Fusion **65**, 016033 (2025).

[15] R. A. Pitts et al., "Physics basis for the first ITER tungsten divertor", Nuclear Materials and Energy **20**, 100696 (2019).

[16] J. Linke et al., "Performance of different tungsten grades under transient thermal loads", Nucl. Fusion **51**, 073017 (2011).

[17] T. Eich et al., "ELM divertor peak energy fluence scaling to ITER with data from JET, MAST and ASDEX upgrade", Nuclear Materials and Energy **12**, Proceedings of the 22nd International Conference on Plasma Surface Interactions 2016, 22nd PSI, 84–90 (2017).

[18] M. Komm et al., "Mitigation of divertor edge localised mode power loading by impurity seeding", Nuclear Fusion **63**, 126018 (2023).

[19] J. Flanagan et al., "ELM buffering in the MAST Upgrade Super-X divertor", Nuclear Fusion **65**, 10.1088/1741-4326/ae11c5 (2025).

[20] I. T. Chapman and et al., "Sawtooth control and impact in MAST", Nuclear Fusion **50**, 045007 (2010).

[21] A. Kallenbach and et al., "Divertor power load feedback with nitrogen seeding in ASDEX Upgrade", Plasma Physics and Controlled Fusion **52**, 055002 (2010).

[22] S. Henderson et al., "Divertor detachment and reattachment with mixed impurity seeding on ASDEX Upgrade", Nuclear Fusion **63**, 086024 (2023).

[23] L. Kogan et al., "First mast-u equilibrium reconstructions using the efit++ code", English, in 48th eps conference on plasma physics 27 june - 1 july 2022, Europhysics conference abstracts (2022).

[24] A. R. Field et al., "The influence of gas fuelling location on H-mode access in the MAST spherical tokamak", Plasma Physics and Controlled Fusion **46**, 981–1007 (2004).

[25] J. M. Stobbs, A. Tookey, A. J. Thornton, T. Farley, and the MAST-U Team, "The infrared thermography system on the MAST-U tokamak", Review of Scientific Instruments **95**, 113509 (2024).

[26]J. G. Clark et al., "First divertor Thomson scattering measurements on MAST-U", Review of Scientific Instruments **93**, 103534 (2022).

[27]J. G. Clark, M. D. Bowden, and R. Scannell, "Low temperature thomson scattering on mast-u", Review of Scientific Instruments **92**, 043545 (2021).

[28]J. Hawke, R. Scannell, J. Harrison, R. Huxford, and P. Bohm, "Outline of optical design and viewing geometry for divertor Thomson scattering on MAST upgrade", Journal of Instrumentation **8**, C11010 (2013).

[29]C. Vincent et al., "Fission Chamber Data Acquisition System for Neutron Flux Measurements on the MAST Upgrade", Review of Scientific Instruments **93**, 093509 (2022).

[30]A. J. Thornton, A. Kirk, and M. Team, "Scaling of the scrape-off layer width during inter-ELM H modes on MAST as measured by infrared thermography", Plasma Physics and Controlled Fusion **56**, 055008 (2014).

[31]S. Henderson et al., "Validating reduced models for detachment onset and reattachment times on MAST-U", Nuclear Materials and Energy **41**, 101765 (2024).

[32]J. W. Berkery et al., "Operational space and performance limiting events in the first physics campaign of MAST-U", Plasma Physics and Controlled Fusion **65**, 045001 (2023).

[33]S. Mijin, D. Power, R. Holden, W. Hornsby, D. Moulton, and F. Militello, "ReMKiT1D: A framework for building reactive multi-fluid models of the tokamak scrape-off layer with coupled electron kinetics in 1D", Computer Physics Communications **300**, Open access under CC BY license; available online 5 April 2024, 109195 (2024).

[34]D. Power, S. Mijin, M. Wigram, F. Militello, and R. J. Kingham, "Scaling laws for electron kinetic effects in tokamak scrape-off layer plasmas", Nuclear Fusion **63**, 086013 (2023).

[35]A. Chankin et al., Plasma Physics and Controlled Fusion **65**, 085003 (2023).

[36]O. V. Batishchev, M. M. Shoucri, A. A. Batishcheva, and I. P. Shkarofsky, "Fully kinetic simulation of coupled plasma and neutral particles in scrape-off layer plasmas of fusion devices", Journal of Plasma Physics **61**, 347–364 (1999).

[37]D. Tskhakaya, R. A. Pitts, W. Fundamenski, T. Eich, S. Kuhn, and J. E. Contributors, "Kinetic simulations of the parallel transport in the JET scrape-off layer", Journal of Nuclear Materials **390–391**, 335–338 (2009).

[38]D. Tskhakaya, F. Subba, X. Bonnin, D. P. Coster, W. Fundamenski, and R. A. Pitts, "On kinetic effects during parallel transport in the SOL", Contributions to Plasma Physics **48**, 89–93 (2008).